

Design and Analysis of Mach-Zehnder and Michelson Interferometers in Silicon on Insulator Platforms

ENRICO M. RENZI^{1,2,*}

¹Physics Program, The Graduate Center, City University of New York, 365 Fifth Avenue, New York, NY 10016, USA.

²Photonics Initiative, Advanced Science Research Center, City University of New York, 85 St. Nicholas Ter, New York, NY 10031, USA.

*erenzi@gradcenter.cuny.edu

Abstract: Silicon photonics offers a scalable solution for high-speed communication systems, with interferometers playing a critical role in modulation, sensing, and data processing. This report investigates Mach-Zehnder (MZI) and Michelson interferometers, fabricated using SOI technology, to determine the free spectral range (FSR) and extract the guided index of waveguides, addressing variability from fabrication imperfections. We modeled and simulated waveguide elements leveraging the SiEPIC-EBeam-PDK library for compact models. Fabrication used the NanoSOI MPW process, and data analysis involved baseline correction, loopback calibration, and Monte Carlo simulations to quantify variability effects. Measurements spanned 1500–1600 nm. Our design achieved a minimal FSR error of 0.74%, within Monte Carlo-predicted variability. Effective indices for MZIs aligned with corrected corner analysis, with an average extracted value of 4.181 compared to the expected 4.204.

1. Introduction

Silicon-on-insulator (SOI) photonics harnesses silicon to create photonic devices for high-speed communication and data processing, effectively addressing traditional electronics' scalability, bandwidth, and power limitations. This technology utilizes a thin silicon layer on a silicon dioxide insulator, enabling the creation of compact, low-loss optical devices due to the high refractive index contrast.

Mach-Zehnder and Michelson interferometers are among the essential devices in silicon photonics. The Mach-Zehnder interferometer (MZI) splits light into two arms, introduces a phase shift to one path, and recombines the beams to create interference. Meanwhile, the Michelson interferometer splits light and reflects it through mirrors before recombination. SOI technology enhances the performance of these interferometers by enabling miniaturization and efficient integration into photonic circuits. In this context, their susceptibility to optical path changes is used to implement optical modulators, biosensors, and metrology applications.

The goal of this work is extracting the strip waveguide group index from measured interferograms of MZI and Michelson interferometers. To do so, we simulate, design and fabricate these interferometers in SOI technology. Multiple variations are designed in order to test the device against fabrication imperfections and variability.

The report is structured to systematically address the design, fabrication, and analysis of Mach-Zehnder and Michelson interferometers in silicon-on-insulator technology. Section 2 introduces the theory of silicon photonics waveguides and key elements such as bends, Y-branches, grating couplers, and interferometers. Section 3 focuses on modeling and simulation, where strip waveguide parameters are extracted using full-wave simulations in Lumerical MODE FDE. The loss introduced by bends is quantified, and each circuit component is simulated using Lumerical Interconnect with the SiEPIC-EBeam-PDK Compact Model Library. This section also includes simulations of the expected performance of the MZI and Michelson interferometers. Section 4 discusses the layout of the tapeout, which was fabricated using the NanoSOI MPW process. Section 5 addresses manufacturing variability, presenting corner analysis and Monte Carlo simulations to evaluate its impact. In Section 6, we provide a

framework for calibrating measurement data to extract the free spectral range (FSR) and effective index from interpolation. Finally, Section 7 wraps up with a discussion of the results and key conclusions.

2. Modelling and Simulation

2.1 Silicon photonics waveguides

Silicon photonics waveguides are optical wires used to guide light. In practice, this is achieved by burying a high-index Si wire (core) with a rectangular cross-section into a low-index material (core), SiO₂, as shown in Fig. 1a, in a configuration called a *strip waveguide*. These devices are usually realized on a Si wafer's thick SiO₂ layer (buried oxide). An effective index characterizes light propagating in optical waveguides, $n_e > 1$, which defines its wavenumber as $\beta = 2\pi n_e / \lambda$ and a group index [1,3]:

$$n_g(\lambda) = n_e(\lambda) - \frac{dn_e(\lambda)}{d\lambda} \lambda, \quad (1)$$

which defines the group velocity as $v_g = c / n_g$.

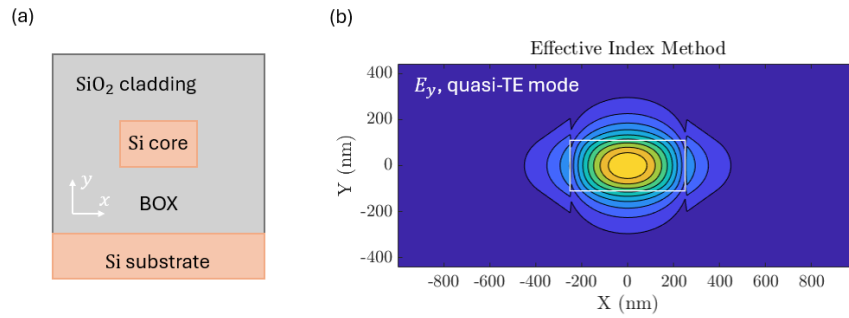


Figure 1: (a) Cross-section view of a strip Si waveguide in SOI technology. A silicon core is deposited on a SiO₂ oxide (BOX) and covered by a SiO₂ core. (b) Electric field y component of a quasi-TE waveguide mode calculated with the effective index method.

The waveguide's height and width determine the number of modes propagating. In a single-mode operation, only one quasi-transverse electric mode (q-TE, with the electric field parallel to the axis) and one quasi-transverse magnetic mode (q-TM, with the electric field parallel to the axis) are guided at the design frequency. The two polarizations have different effective and group indices. The Effective Index Method [3] can be used to calculate an approximate field profile for both polarizations. As shown in Fig. 1b, a TE-polarized wave is strongly confined within the waveguide core.

A compact waveguide model is often used to calculate the effective index of a Si waveguide around a specific working wavelength λ_0 , given by a Taylor series [3]:

$$n_e(\lambda) = n_{e,1} + n_{e,2}(\lambda - \lambda_0) + n_{e,3}(\lambda - \lambda_0)^2, \quad (2)$$

where $n_{e,1}$, $n_{e,2}$ and $n_{e,3}$ are fit parameters obtained from simulation or experiment.

Working temperature changes have an impact on the effective index of a waveguide. The shift in index due to a change in temperature from T_1 to T_2 is given by:

$$\Delta n = -\frac{\partial n_g}{\partial T} \frac{T_2 - T_1}{n(T_1)}, \quad (3)$$

where $\partial n_g / \partial T$ is the thermo-optic coefficient of the waveguide mode [13].

Optical waveguides suffer from a variety of optical losses responsible for signal attenuation. The attenuation constant quantifies the optical loss α , such that the electric field of a mode propagating in the waveguide is given by:

$$E = E_0 e^{i\frac{2\pi}{\lambda} nL} e^{-\frac{\alpha}{2}L} \quad (4)$$

The optical loss is primarily due to the roughness in the waveguide sidewalls due to fabrication processes. The amount of loss depends on the mode shape: q-TE modes have larger losses due to the higher confinement of the electric field compared to q-TM losses [3]. Also, wider waveguides show lower loss. Other sources of loss come from roughness-generated backscattering and radiation. Typical loss values for q-TE and q-TM modes are 1.45 dB/cm and 1.1 dB/cm, respectively, for 500 nm wide waveguide.

2.2 Waveguide bends

Waveguide bends are widely used in Si-integrated circuits. Radiation and mode mismatch losses arise because light propagating in a bend is pushed toward the waveguide walls. The former is due to abrupt discontinuities in the waveguide and can be reduced by employing a large enough bending radius to smooth the transition. Radiation losses are usually lower for q-TE modes than q-TM modes, which are less confined, more prone to radiate, and require a larger bending radius. On the other hand, mode mismatch losses are equally important for both polarizations and can be reduced using Bezier curves [3].

2.3 Y-branches splitters and combiners

A Y-branch splitter operates by dividing an incoming optical signal into two or more output paths, while a combiner performs the reverse, merging light from multiple inputs into a single output [3]. These structures are typically fabricated in silicon waveguides by tapering a single waveguide into two branches, carefully designed to minimize losses and ensure efficient power distribution. Due to the high refractive index contrast between silicon (waveguide core) and silicon dioxide (cladding), Y-branches in Si waveguides can achieve compact designs while maintaining low insertion loss. However, due to mode mismatch and waveguide geometry, care must be taken to reduce potential scattering or reflection at the branching points. In silicon photonic systems, these components are essential for constructing more complex optical circuits, such as Mach-Zehnder interferometers, multiplexers, and power splitters.

2.4 Fiber grating couplers

Grating couplers enable light coupling between optical fibers and silicon waveguides. Fully etched grating couplers are cost-effective and well-suited for rapid prototyping [5] at the cost of low coupling efficiency and bandwidth. They are designed to couple incoming fiber optics light at an off-normal angle to minimize back-reflection losses and maximize the coupling with the target waveguide mode. Sub-wavelength grating couplers (SWGCs) utilize sub-wavelength grating lines to provide improved performance, reduce reflections, and increase coupling efficiency [3,5]. These designs also offer broader bandwidth and lower back reflection than regular fully-etched grating couplers. Experimental results demonstrate that for a transverse electric (TE) mode at 1550 nm, insertion loss is -4.05 dB with a 52.3 nm 3-dB bandwidth, while for a transverse magnetic (TM) mode, insertion loss is -3.74 dB with an 81.5 nm 3-dB bandwidth.

2.5 The Mach-Zehnder interferometer

A Mach-Zehnder interferometer (MZI) is a two-port device in which an input light pulse is sent by a beam splitter into two waveguides and then recombined by a beam combiner at an output. Suppose the two paths have identical geometrical and material properties. Then we have a *balanced* MZI (Fig. 2a). In this case, the two beams constructively interfere for any frequency at the output port because of the same phase accumulation by the pulses traveling in the two branches. On the other hand, if the two paths differ by geometry or material parameters, we have an *unbalanced* MZI. In this case, the output signal will show a frequency-dependent interference pattern that can be constructive or completely destructive.

In this work, we consider the unbalanced MZI scheme in Fig. 2b. Two paths with lengths L_1 and L_2 , respectively, are designed to differ by an amount $\Delta L = L_1 - L_2$. The waveguides have effective indexes $n_{e,1}$ and $n_{e,2}$, and attenuation constants α_1 and α_2 , respectively.

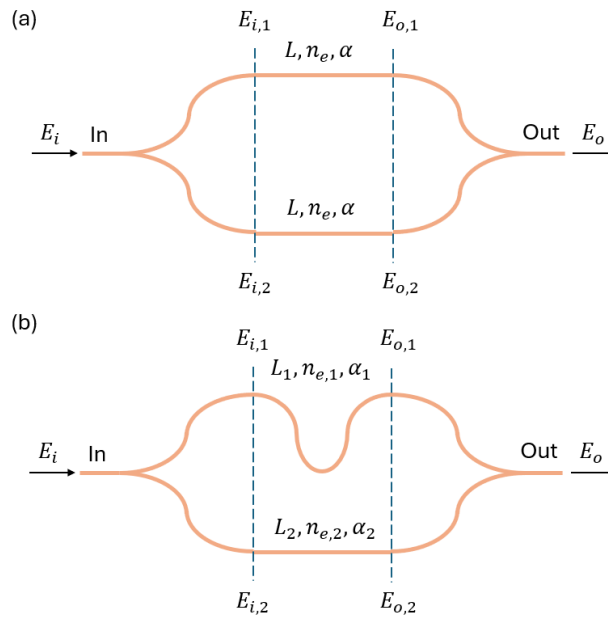


Figure 2: Schematic view of an (a) balanced and (b) unbalanced Mach-Zehnder Interferometer.

Without loss of generality, we consider a guided TE mode, whose vector field is $\mathbf{E} = \hat{\mathbf{y}}E_i$. Upon injecting the mode, the input field is split equally in the two waveguides such that after the beam splitter:

$$E_{i,1} = E_{i,2} = \frac{E_i}{\sqrt{2}}. \quad (5)$$

Then, each waveguide introduces both phase shift and amplitude decay. Therefore, the output intensity is given by:

$$I_o = \frac{E_i^2}{4} \left| \exp(i\beta_1 L_1) \exp(-\alpha_1 L_1) + \exp(i\beta_2 L_2) \exp(-\alpha_2 L_2) \right|^2. \quad (6)$$

For simplicity, we may assume zero material loss, such that $\alpha_1 = \alpha_2 = 0$ and effective mode indexes $\beta_1 = \beta_2 = \beta$, the expression above may be simplified in the useful MZI interferometer transfer function:

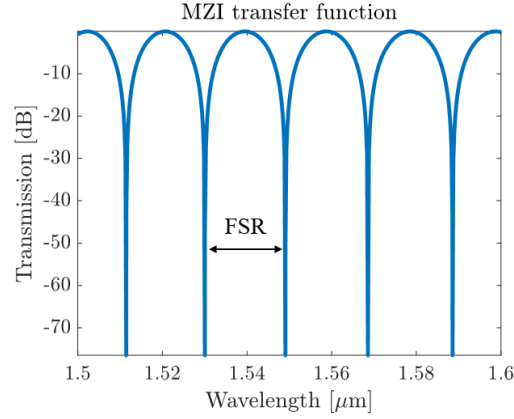


Figure 3: Transfer function of an MZI having $\Delta L = 30 \mu\text{m}$.

$$\frac{I_o}{I_i} = \frac{1}{2} [1 + \cos(\beta \Delta L)] \quad (7)$$

The transmission transfer function (7) for an ideal (i.e., lossless) interferometer with $\Delta L = 30 \mu\text{m}$ is plotted in Fig. 3. The distance between peaks, called *free spectral range* (FSR), is calculated assuming that the phase difference between contiguous peaks is $2\pi = (\beta_{i+1} - \beta_i) \Delta L$ [3], and is:

$$\text{FSR}(\lambda) = \frac{\lambda^2}{\Delta L n_g(\lambda)}, \quad (8)$$

where $n_g(\lambda)$ is the dispersive mode group index Eq. (1). Because the FSR is a function of the mode group index $n_g(\lambda)$, in the following we will use this dependency to extract this quantity from simulation and experimental data.

2.6 The Michelson Interferometer

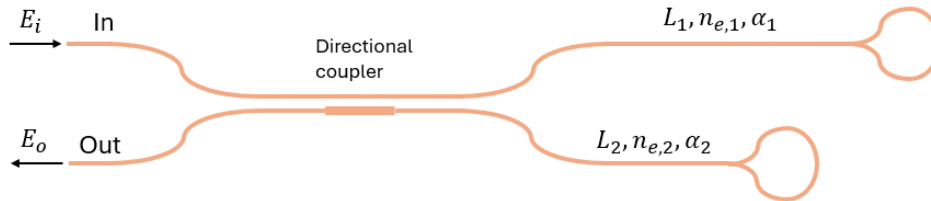


Figure 4: Schematic view of an unbalanced Michelson Interferometer.

Fig. 4 illustrates the typical scheme of a Michelson interferometer realized on SOI [6]. This device's working principle requires one beam splitter and two mirrors. Light is injected, split into two branches, reflected to the splitter, and recombined. No interference pattern is observed at every frequency if the two branches are identical. However, an interferogram emerges like in the MZI if an imbalance is introduced. Because light propagates twice along each branch, the phase accumulated by the interferometer is twice that of an MZI with the same branch

lengths and waveguide geometry. Then, considering an ideal interferometer with a homogeneous effective mode index, the transfer function is:

$$\frac{I_o}{I_i} = \frac{1}{2} [1 + \cos(2\beta \Delta L)], \quad (9)$$

where $\beta = 2\pi n_e / \lambda$ and $\Delta L = L_2 - L_1$. Because the interferometer shows twice the efficiency of an MZI, the FSR is halved, having:

$$\text{FSR}(\lambda) = \frac{1}{2} \frac{\lambda^2}{\Delta L n_g(\lambda)}. \quad (10)$$

The design of this interferometer requires extra elements compared to an MZI. In fact, the input port is connected to an adiabatic 50:50 directional coupler to split the input signal. This element, in fact, acts both as a 50:50 beam splitter and as a beam combiner that merges the two beams sending the signal to the output port. Moreover, each branch terminates on a waveguide loop connected by two Y-branches to the interferometer.

3. Modelling and Simulation

3.1 Silicon on Insulator Waveguides

This work uses a Si waveguide with a rectangular cross-section (Fig. 1a). We choose dispersive materials for the waveguide's core and cladding, namely Si-Palik and SiO₂-Palik, both available in the Ansys Optics simulation software [7]. The chosen height is $h = 220$ nm, which is a standard in Si photonics industry [3], whereas the width is $w = 500$ nm, both ensuring that the waveguide remains nearly single mode near the center working wavelength, i.e., $\lambda_0 = 1550$ nm. Moreover, the used combination of height and width is convenient in terms of design, as most devices available in the SiEPIC-EBeam-PDK Compact Model Library [8] are optimized for this size.

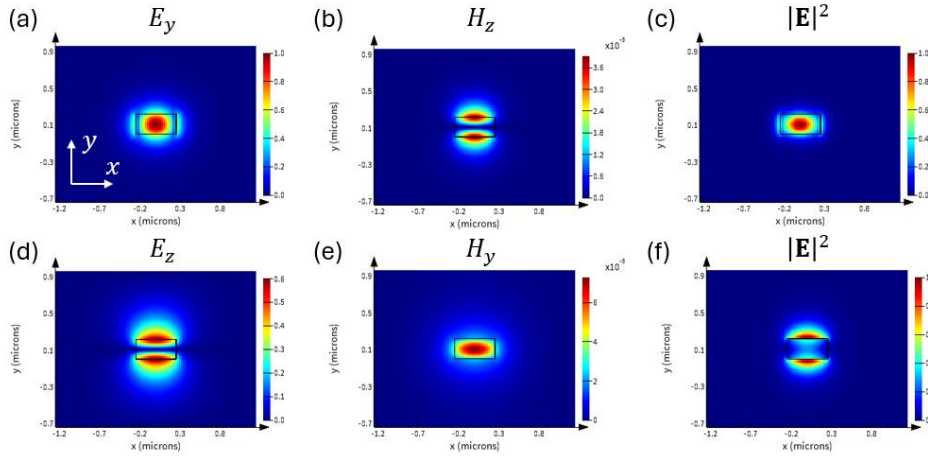


Figure 5: (a-b) Field map and (c) intensity for a fundamental quasi-TE mode propagating in Si waveguide with height 220 nm and width 500 nm. (d-f) Field map and (c) intensity for a fundamental quasi-TM mode. The working wavelength is 1550 nm. The simulations have been performed with the Lumerical FDE solver.

Without loss of generality, we will focus on TE waveguides. A field map of the main field components of the guided quasi-TE modes is reported in Fig. 5a-c. This field maps agree with that obtained with the effective index method reported in Fig. 1b. For completeness, we also report the field map for a quasi-TM mode guided by the same waveguide in Fig. 5d-f. The full

wave simulations have been run on the Lumerical MODE Finite Difference Eigen-mode (FDE) solver [9]. Comparing Fig 5c and d, the electric field of the q-TE mode looks more confined than the one of the q-TM mode.

To correctly characterize the waveguide dispersion at the working frequency, we perform a modal analysis and extract the effective and group index for the first two fundamental modes. The extracted values for the effective and group index at λ_0 are reported in Table 1. Note that because of the very low material loss in the waveguide, the imaginary part of the indexes is neglected. The higher confinement of the q-TE mode is translated into a larger effective index than the q-TM mode.

Table 1. Extracted effective and group indexes for a 220 nm × 500 nm Si waveguide at $\lambda_0=1550$ nm.

Mode	Effective Index, n_e	Guided Index, n_g
Fundamental TE	2.443	4.056
Fundamental TM	1.768	3.634

Using Eq. (2), we extract the waveguide compact model parameter in the wavelength range [1500,1600] nm. The fit parameters are reported in Table 2 for both fundamental modes' effective and group indexes.

Table 2. Compact waveguide model parameters for a 220 nm × 500 nm Si waveguide at $\lambda_0=1550$ nm.

Mode	Index	n_1	n_2 [1/ μm]	n_3 [1/ μm^2]
Fundamental TE	n_e	2.447	-1.134	-0.0410
	n_g	4.0558	0.451	-0.0511
Fundamental TM	n_e	1.768	-1.198	0.915
	n_g	3.632	-5.223	-7.300

The fit function plotted against the simulation data is reported in Fig. 6.

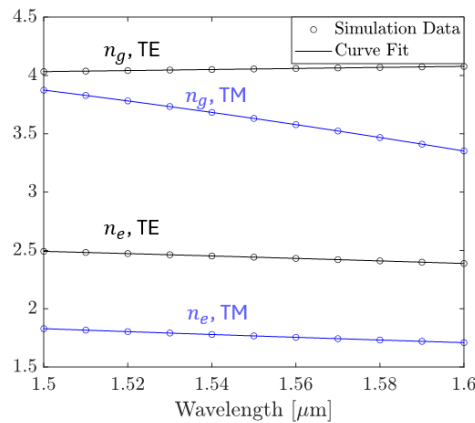


Figure 6: Dispersion of the effective and group index from modal analysis and from fit model with the data reported in Table 2. The index dispersion is plotted for both q-TE (black) and q-TM (blue) modes.

3.2 Waveguide bends

In our design, we employ waveguide bends with a 5- μm radius, which are a standard in Si photonics design for q-TE waveguides. We perform a modal analysis in Lumerical FDE and find that the used bend introduces a total loss of 5.51 dB/cm with a total mode overlap equal to 0.99881. This mismatch is due to the mode pushed toward the waveguide boundary by the bend, as shown in Fig. 7.

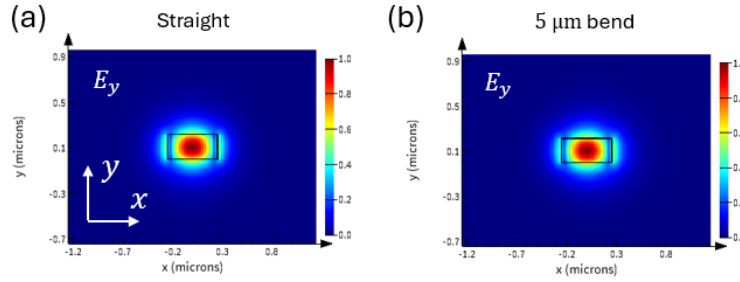


Figure 7: When a (a) straight waveguide is bent, the guided mode is (b) pushed toward the boundary. The simulation is run for $\lambda = 1.55 \mu\text{m}$ and a 5 μm bending radius.

3.3 Grating Coupler, Y-branch and Broadband Directional Coupler

In the following, we simulate the set of components that we use in the design of the Mach-Zehnder and Michelson interferometer. These simulations are performed using Lumerical Interconnect [REF], which allows us to use the SiPEC-EBeam-PDK library provided in the course. This library embeds a set of compact models with scattering parameters for the most widely used Si-photonics devices extracted from experiments.

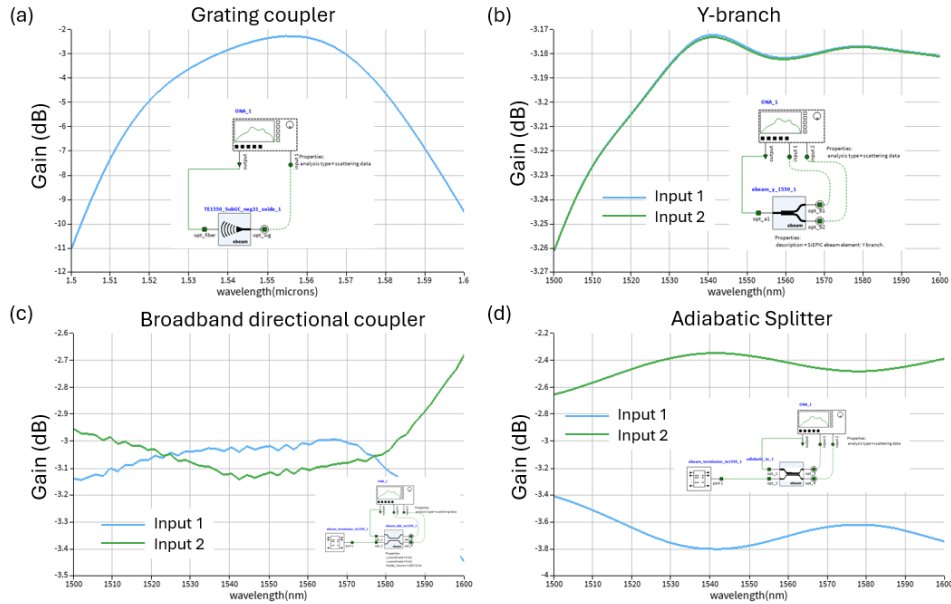


Figure 8: Simulation in Lumerical Interconnect of a (a) grating coupler, (b) Y-branch, (c) broadband directional coupler, and (d) adiabatic coupler. The simulation scheme of each component is reported as an inset in each panel. Simulations are performed with Lumerical Interconnect using the SiPEC-Ebeam-PDK library.

Light is coupled from an optic fiber to the circuit by means of a grating coupler. Fig.8a reports the simulation of this coupler. This component is expected to introduce a minimal 2.5dB insertion loss at $\lambda_0 = 1.55 \mu\text{m}$, due to the coupling mismatch between optic fiber and grating and radiation loss in the SiO_2 substrate.

Next, we simulate a Y-branch that evenly splits power between two waveguides. The simulation in Fig.8b shows a gain of -3.18 dB for both paths, with an almost flat bandwidth in the vicinity of λ_0 .

The Michelson interferometer uses a broadband directional coupler to isolate the input path from the output. From our simulations of this device (Fig. 8c), we expect the component to introduce a slightly uneven insertion loss for the two different paths. This difference is due to the element's non-idealities due to fabrication defects and optimization limitations.

In our design, we compare the performance of the Y-branch used as a beam combiner with that of an adiabatic splitter. The latter should minimize radiation loss when two paths are joined. The simulation shown in Fig. 8d shows that this component is non-ideal, with uneven insertion loss for the two output paths. However, it shows a better flat broadband response than the Y-branch.

3.4 The Mach-Zehnder Interferometer

A Mach-Zehnder interferometer is simulated in Lumerical Interconnect. A schematic of the Interferometer is shown in Fig. 9. The input and output ports of the MZI are connected to an optical network analyzer by means of two fiber grating couplers optimized to have minimal insertion loss at $\lambda_0 = 1550 \text{ nm}$. The MZI's unbalance is realized by choosing a different waveguide length for the two arms. The transfer function of the MZI is plotted in Fig. 10a (light blue line) for a path difference $\Delta L = 109.250 \mu\text{m}$, showing a minimal insertion loss of -25 dB and a free spectral range equal to 5.51 nm .

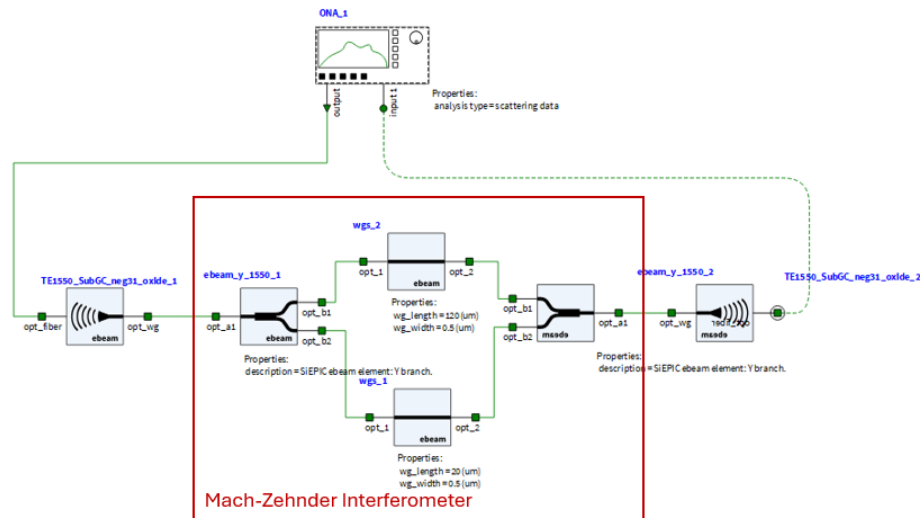


Figure 9: Simulation of a MZI in Lumerical Interconnect. Fiber grating couplers connect the interferometer (red box) to an optical network analyzer.

We test a different variation of the interferometer using an adiabatic combiner at the output port (Fig. 10a, green line), which shows a smaller FSR and insertion loss down to -40 dB . This result is explained by the lower insertion loss introduced by the adiabatic combiner, which avoids radiation loss and mode mismatch at the output.

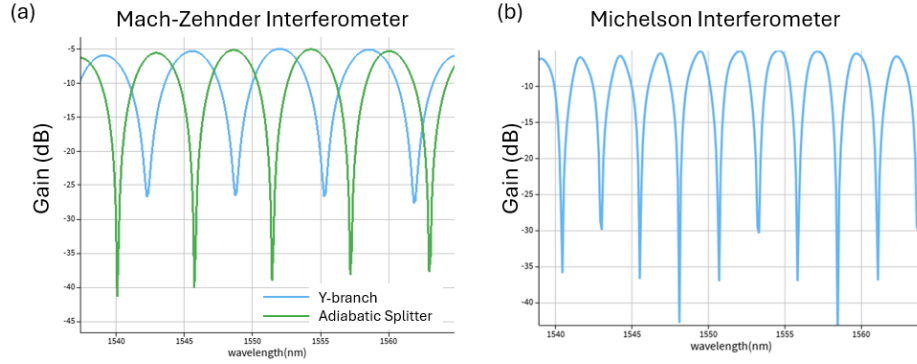


Figure 10. (a) Transfer function of a MZI with path difference $\Delta L = 109.250$ nm and using an output Y-branch combiner (blue) and adiabatic combiner (green); (a) Transfer function of a Michelson interferometer having path difference $\Delta L = 109.250$ nm. For the same path difference, the Michelson interferometer shows half the FSR.

As predicted by theory, a longer path difference decreases the MZI FSR. This result is shown in Fig. 11 (black line) and compared with simulation data (black crosses). The FSR is calculated at $\lambda = 1550$ nm, considering $n_g = 4.22$.

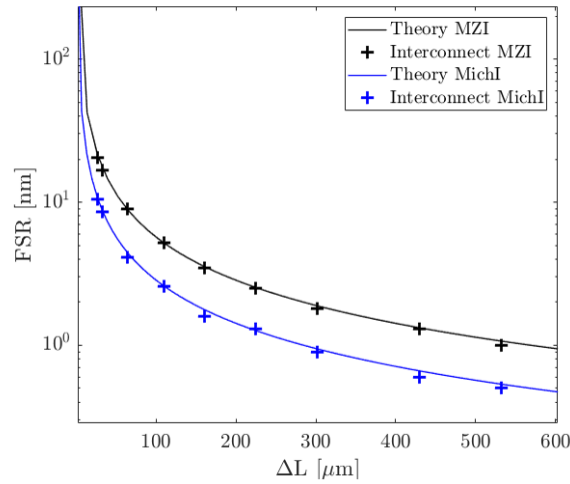


Figure 11: Theory (solid line) and simulated (crosses) FSRs for MZI (black) and Michelson (blue) interferometers. With increasing path difference ΔL , the FSR is reduced with the Michelson interferometer showing double efficiency compared to the MZI.

3.5 The Michelson Interferometer

A Michelson interferometer is designed and simulated in Lumerical Interconnect (Fig. 12). This design uses a broadband directional coupler to evenly split the input signal into two branches having different lengths. Each branch is terminated by an ideal loop realized using a $10 \mu\text{m}$ strip waveguide connected to a beam-splitter/combiner.

Fig. 11 reports the interferometer's FSR for different path length differences. Theory (blue line) and simulation (blue crosses) agree. We observe that the Michelson Interferometer shows half the FSR of an MZI with the same path difference.

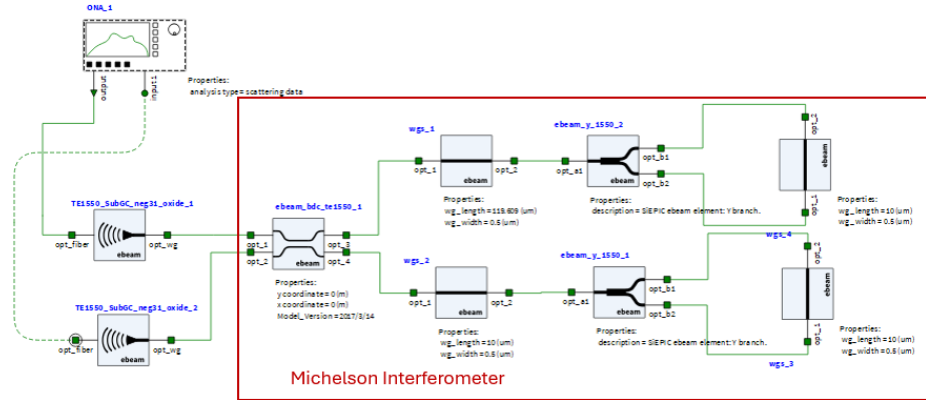


Figure 12: Simulation of Michelson interferometer in Lumerical Interconnect. Fiber grating couplers connect the interferometer (red box) to an optical network analyzer. The beam splitting and recombination are performed by a broadband directional coupler.

4. Layout

The proposed tape-out realized in KLayout [10], is shown in Fig. 13. This design contains one reference TE strip waveguide, 8 MZI and 5 Michelson interferometers. The details regarding the geometry and the expected FSRs of the devices are reported in Table 3. To satisfy the foundry requirements, the whole area is contained in $605\ \mu\text{m} \times 410\ \mu\text{m}$ rectangular box. The grating couplers are oriented to allow the correct coupling with the optic waveguide used in the Maple Leaf Photonics automated probe station [11,12].

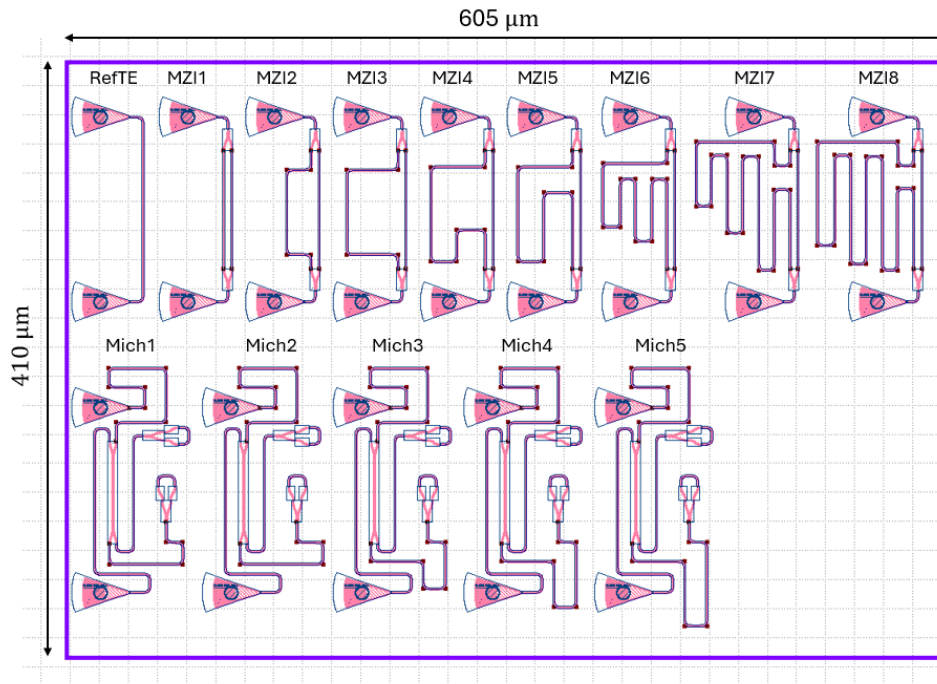


Figure 13: designed layout.

Table 3. Layout parameter for the tape-out in Fig. 13.

Label	Component	ΔL [μm]
RefTE	Strip waveguide	n/a
MZI1	MZI	0
MZI2	MZI	27.276
MZI3	MZI	64.374
MZI4	MZI	109.609
MZI5	MZI	160.890
MZI6	MZI	224.993
MZI7	MZI	423.921
MZI8	MZI	526.535
Mich1	Michelson	0
Mich2	Michelson	12.986
Mich3	Michelson	32.226
Mich4	Michelson	57.879
Mich5	Michelson	83.533

The number of devices allows to investigate manufacturing variability in effective index and free spectral range, with each device oriented vertically for testing, grating couplers positioned on the left (upper as input and lower as output), and a minimum spacing between elements of 60 μm to prevent accidental probing and maximize isolation. The grating couplers were oriented to the right to avoid chip rotations, and a 127 μm pitch was set for input and output gratings to align with the fiber array. To mitigate bend losses, TE-device curves have a 5 μm radius.

5. Manufacturing variations

Manufacturing challenges in silicon photonics primarily stem from variability during fabrication processes, which affect device performance and yield. Silicon thickness variations in SOI wafers, often within a ± 5 nm range, significantly influence the effective index. Feature size variability, caused by inconsistencies in resist thickness, exposure, development, and etching, adds further uncertainty. Systematic issues like lithographic smoothing and process drift, along with random variations, result in deviations both within a single chip and across chips in a wafer. These discrepancies can manifest as wavelength mismatches, free spectral range inconsistencies, and increased optical losses in devices.

To account for fabrication variability, we implement a corner analysis to evaluate the performance of photonic devices under extreme process variations. The analysis involves systematically varying critical geometric parameters, specifically the waveguide width and height, within the typical variation range of the NanoSOI MPW fabrication process by Applied Nanotools. For this platform, the nominal waveguide width is 500 nm, with a tolerance of $+10/-30$ nm, while the nominal waveguide height is 220 nm, with a variation of $+3.1/-4.7$ nm. These tolerances define the "corners" for the analysis, representing combinations of maximum and minimum values for each parameter.

After postprocessing the data, we realized that the initial corners were not optimal to include the range of variability of the measured effective index and free spectral range. To address this, we expanded the range of the waveguide width to better capture the variability observed in these devices. The revised corners for the MZI fabrication are defined as follows:

- Waveguide width: 495 ± 25 nm (ranging from 470 nm to 520 nm).
- Waveguide height: 219.2 ± 3.9 nm (ranging from 215.3 nm to 223.1 nm).

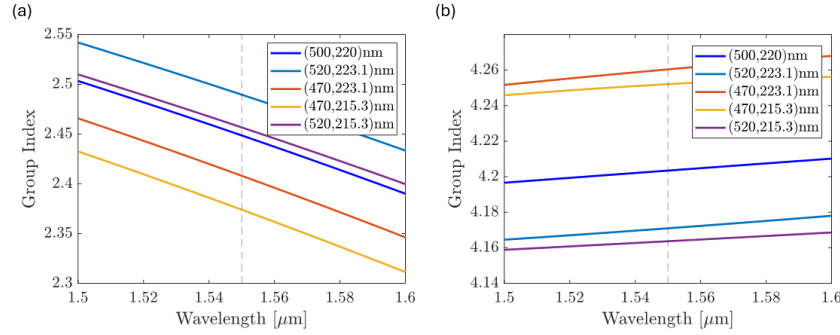


Figure 14: Corner analysis for the waveguide (a) effective index and (b) group index. The index dispersion for the waveguide width (500 nm) and height (220 nm) nominal value is reported in blue.

The related corners for effective index and group index are reported in Fig. 14. We used these revised corners to predict the variation in the free spectral range (FSR) for MZI4 with $\Delta L=109.609\mu\text{m}$ and nominal waveguide dimensions of $(W,h)=(500,220)$ nm. The result of this analysis is shown in Fig. 15.

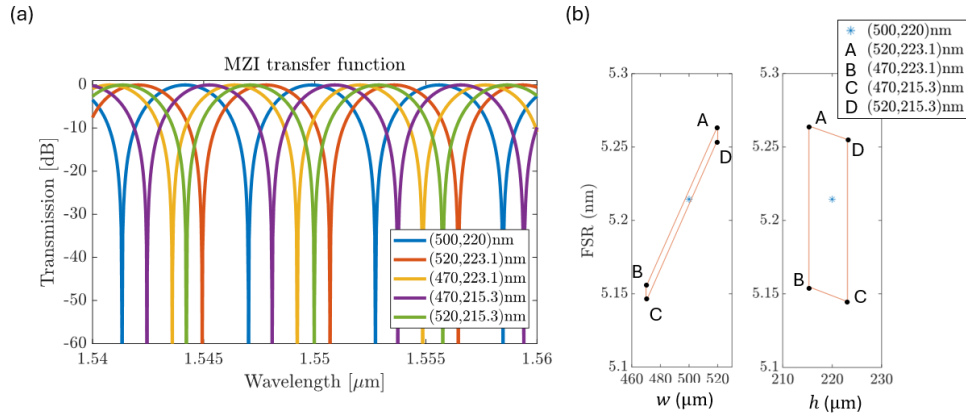


Figure 15: (a) Corner analysis for the transfer function for MZI4 ($\Delta L = 109.609 \mu\text{m}$) and (b) respective FSR. A blue star indicates the nominal value.

While corner analysis provides the extrema of variability, it does not capture the probabilistic nature of manufacturing deviations. Therefore, we performed a Monte-Carlo simulation to predict the variability using a stochastic approach. This analysis was based on the circuit design shown in Fig. 13, which also includes the presence of grating couplers, Y-junctions and bends. The analysis was implemented using the Monte-Carlo simulation tool [13] in the SiPEC-EBeam-PDK library. By simulating 100 samples for the MZI4 design (Fig. 16), we predicted a mean FSR of 5.14 nm with a standard deviation of 0.0091 nm, with an average insertion loss of 5.26 dB and standard deviation of 0.0709 dB.

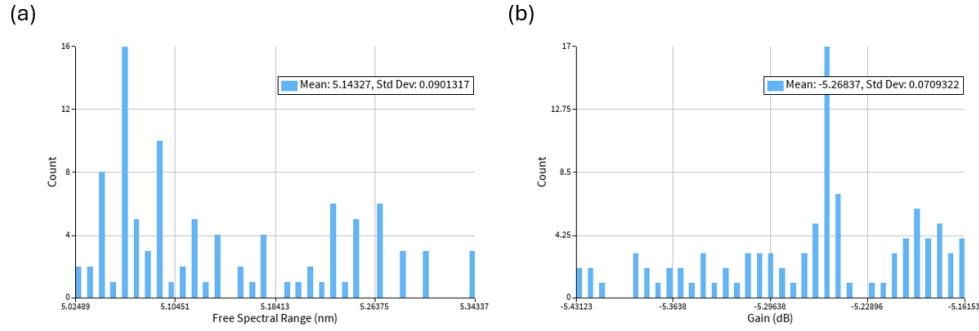


Figure 16: Monte-Carlo simulation quantifying the variability of (a) the FSR and (b) insertion loss for the device MZI4 ($\Delta L = 109.609 \mu\text{m}$).

6. Measurement data analysis

6.1 Baseline correction and loopback calibration

We analyzed all the Mach-Zehnder (MZI) and Michelson interferometers, but in the following, we report results for MZI4 and Mich4 as representative cases. The measured spectra are shown in Fig. 17a for MZI4 and Fig. 17b for Mich4. Both spectra exhibit higher losses than predicted by simulations. These losses are attributed to the narrowband nature of the grating couplers, coupling losses in the measurement setup, manufacturing variability, and bend losses within the devices.

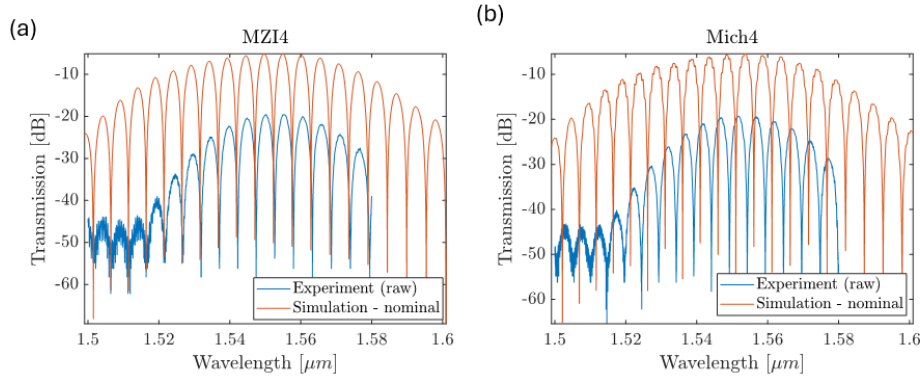


Figure 17: (a) MZI4 simulation data (red) vs experimental raw data (blue). (b) Mich4 simulation data (red) vs experimental raw data (blue).

Before extracting the group index and free spectral range, it is necessary to isolate the intrinsic frequency response of the interferometers. Two methods are considered: baseline correction and loopback calibration.

- **Baseline Correction:** This method involves fitting the spectrum using a low-order polynomial to approximate the baseline response of the grating couplers and subtracting it from the measured data. However, the process is suboptimal as the choice of the polynomial function is arbitrary, potentially introducing inaccuracies.
- **Loopback Calibration:** This approach uses a calibration device, such as a loopback structure or an interferometer with $\Delta L=0$, to measure and correct for systematic losses. The calibration response is then subtracted from the measured spectrum for normalization.

The results of baseline correction are presented in Fig. 18a,b for MZI4 and Fig. 18c,d for Mich4, obtained using a 4th order interpolant function (red).

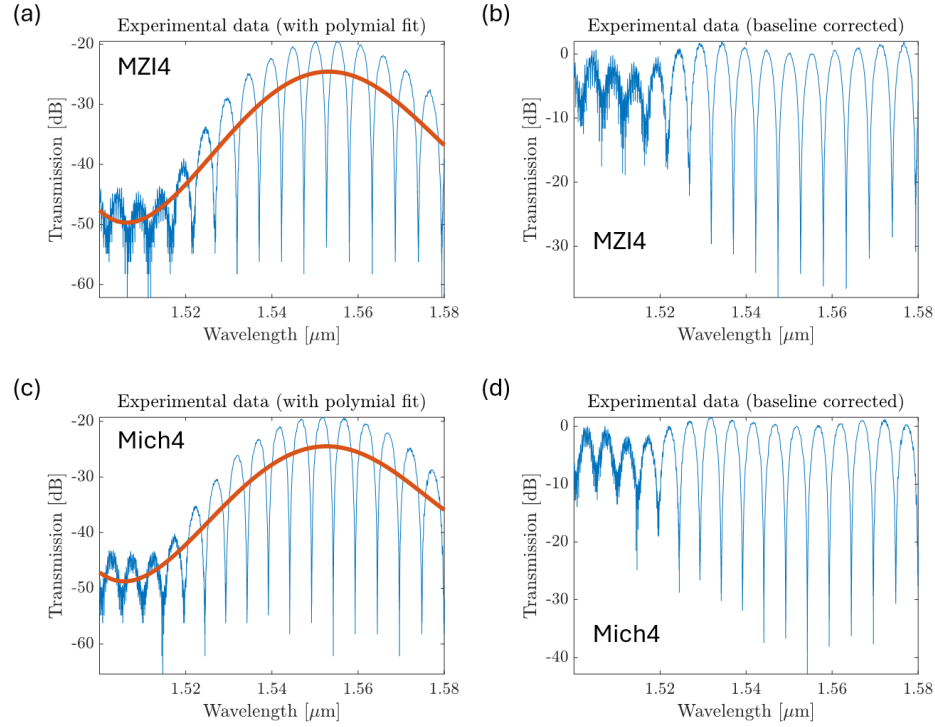


Figure 18: (a) Baseline interpolation (red) of the raw data (blue) and (b) resulting corrected spectrum for MZI4. (c) Baseline interpolation (red) of the raw data (blue) and (b) resulting corrected spectrum for Mich4.

While the baseline correction provides some insights on the amount of loss in the system, its arbitrary nature limits its effectiveness. Moreover, we note that this method does not allow to completely isolate the interferometer spectrum and obtain a non-dispersive response.

The loopback calibration results are shown in [Fig. 19a,b](#) for MZI4 and [Fig. 19c,d](#) for Mich4. For MZI4, the response after calibration is significantly flatter, demonstrating successful normalization with the calibration data from Mich1. However, for Mich4, the calibration is less effective. This discrepancy is likely due to the narrowband response of the directional coupler and the excessive number of meanders in the Michelson interferometer design.

6.2 Fitting MZI and Michelson interferometer data

The function to fit the MZI data is

$$F = 10 \log_{10} \left(\frac{1}{4} \left| 1 + \exp \left[-i \frac{2\pi n_{eff}}{\lambda} (2)\Delta L - \frac{1}{2} \alpha (2)\Delta L \right] \right|^2 \right) + b \quad (11)$$

Where ΔL is the optimal waveguide path mismatch, λ the working wavelength, α is the waveguide loss and b a fitting parameter representing the excess loss of the device. Notice that the 2 factor is only used while fitting Michelson data. The effective index, n_{eff} , is represented using (2), for which $n_{e,j}$, $j = 1, 2, 3$ are unknown fitting parameters. The fit is performed using the least square curve fitting method, where we minimize the difference between the measured data and the model in (11).

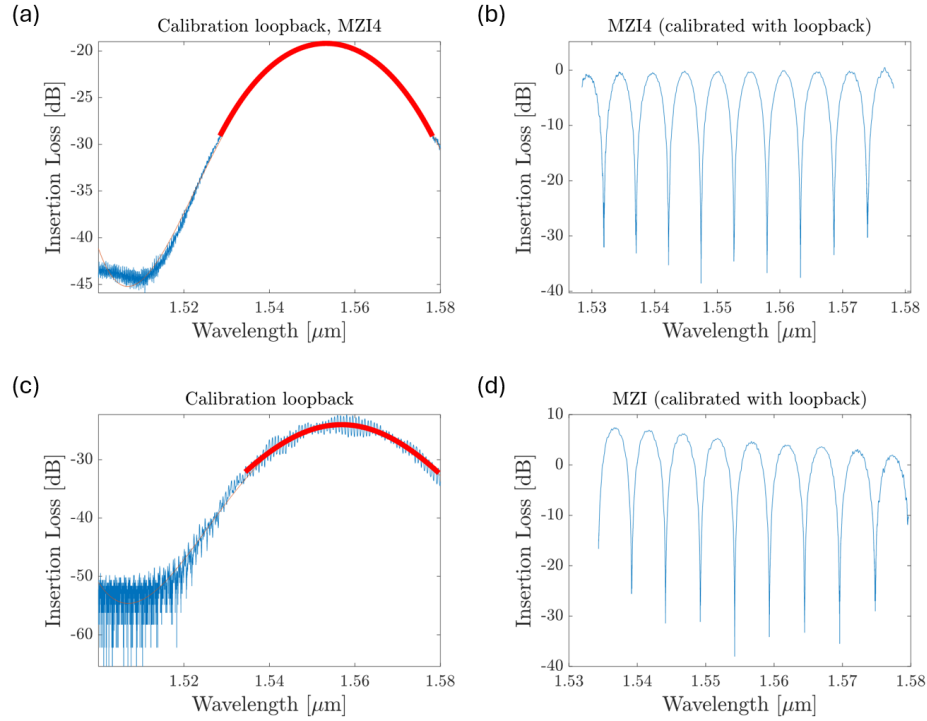


Figure 19 (a) Loopback interpolation (red) of the MZI1 reference spectrum data and (b) resulting corrected spectrum for MZI4. (a) Loopback interpolation (red) of the Mich1 spectrum data (b) resulting corrected spectrum for Mich4.

Upon interpolations, we may find the waveguide group index as

$$n_g = n_e - \lambda \frac{dn_e}{d\lambda} = n_1 - n_2 \lambda_0 \quad (12)$$

and the group velocity dispersion as

$$D = -\frac{\lambda}{c} \frac{d^2 n}{d\lambda^2} = -\frac{\lambda}{c} 2n_3 \quad (13)$$

This method requires a careful choice of the initial guess. First, the FSR is determined using a curve-fitting autocorrelation to find the correct periodicity and determine the right initial guess. This is performed by shifting and multiplying the spectra with its copy. When the signals are shifted by exactly one period, the autocorrelation function shows a maximum. This value corresponds to the free spectral range of the interferometer. To determine the horizontal correction, we calculate the cross-correlation of the signal. Hence, we proceed with the method above to determine the waveguide parameters. Then, we obtain:

$$FSR[n] = \lambda_{n+1} - \lambda_n \quad (14)$$

from which we determine

$$n_g = \frac{\lambda^2}{FSR[n](2)\Delta L} \quad (15)$$

where ΔL is known (the 2 factor is used only for Michelson data). Then, we find the effective index by matching the middle dip in the spectrum to determine n_1 , which is responsible for the horizontal shift of the spectrum.

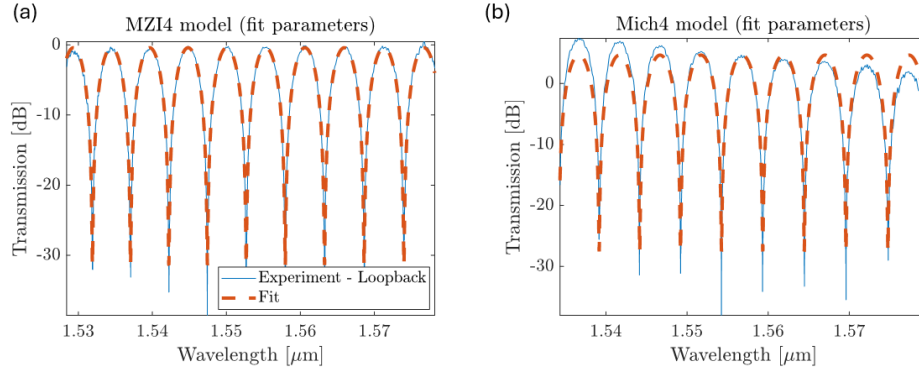


Figure 20: Loopback corrected measurement data vs simulated fit for (a) MZI4 and (b) Mich4.

For a minimum located at λ_0 , we know from (7) that

$$\frac{2n_1\Delta L}{\lambda_0} = 2N + 1 \quad (16)$$

and hence we can find the mode number N by inverting and rounding after inserting an initial guess for $n_{1,0} \simeq 2.44$ (for a TE mode). With the correct mode number, we can find n_1 . With this information, we can find n_2 as

$$n_2 = -\frac{n_g - n_1}{\lambda_0} \quad (17)$$

For highly dispersive modes, such as TM modes, we need to provide a correct estimate for the index n_3 . Otherwise, this index can be set equal to zero.

An example comparing interpolated data with experimental data is shown in Fig. 20a for MZI4 and Fig. 20b for Mich4. The effective index model data for these devices are summarized in Table 4 for MZI and Table 5 for Michelson interferometers, while the extracted FSRs data are presented in Table 6.

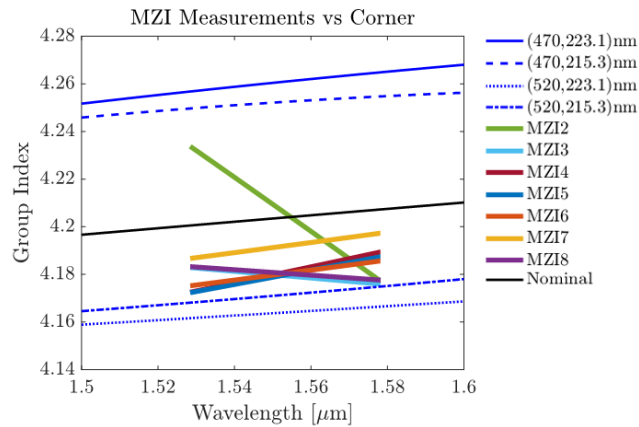


Figure 21: For the MZI series, the compact model for different corners (blue lines) is compared with experimental data (colored lines) and nominal dispersion (black), obtained using a width of 500 nm and height of 220nm, respectively.

For the MZI data, the loopback correction demonstrates excellent agreement between the simulated and experimental data, with a minimal FSR error of 0.74% observed for MZI7. This error falls well within the variation predicted by the Monte-Carlo simulation. We observe a general improvement in the FSR prediction accuracy as the path difference increases. Furthermore, the extracted effective index values lie within the bounds established by the corner analysis in Fig. 14a, which were adjusted to account for actual process variability. The average extracted effective index is 4.181, closely matching the expected value of 4.204. According to the corner analysis, this slight discrepancy suggests that the fabrication process tends to produce slightly wider and thicker waveguides. These larger waveguides yield a higher group index, as the optical modes are less confined within the waveguide.

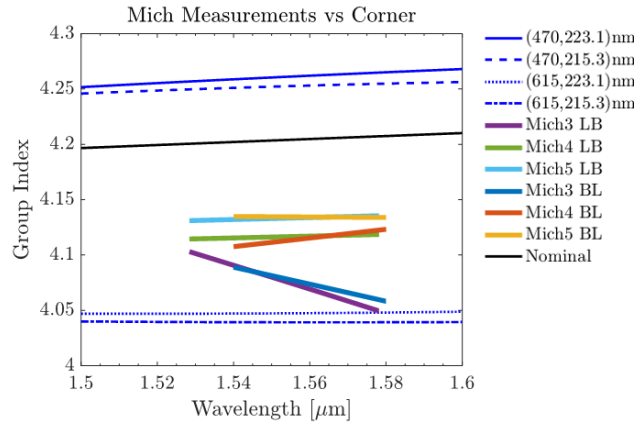


Figure 22: For the Michelson series, the compact model for different corners (blue lines) is compared with experimental data (colored lines) and nominal dispersion (black), obtained using a width of 500 nm and height of 220nm, respectively.

In contrast, the Michelson interferometer data for small path differences deviate significantly from the expected values. The measurement data for Michelson devices was noisier, which negatively impacted the quality of the interpolation. Additionally, the reference circuit used for baseline correction did not function as expected, leading to inaccurate corrections. For completeness, we provide both baseline and loopback correction fits for these circuits. While both methods yield consistent values for the effective index and group index, they differ significantly in their estimates for dispersion and residual insertion loss (bbb).

Although the extracted effective index aligns with the corner analysis predictions, the group index shows a larger mismatch compared to the MZI results. Specifically, the measured group index for the Michelson interferometers is smaller than expected. To address this, the maximum waveguide width in the corner analysis was extended to 615 nm. This adjustment, however, might not reflect actual fabrication variability but instead parasitic effects introduced by the Michelson interferometer's meandered structure and loops.

In this design, we aimed to maximize the compactness of the circuit. However, this approach may be suboptimal for Michelson interferometers, as it likely introduces additional dispersion and coupling losses, leading to the observed discrepancies.

Table 4. MZI interpolation data for effective index model extracted from measurements.

Label	n_1	n_2	n_3	α	b	R	n_g at $1.55\mu m$
Theory	2.449	-1.133	-0.775				4.204
MZI2	2.443	-1.135	0.366	4.001e-3	0.130	0.996	4.208
MZI3	2.419	-1.133	0.0450	1.898e-3	0.0138	0.990	4.180
MZI4	2.400	-1.146	-0.109	1.031e-3	-0.154	0.995	4.179
MZI5	2.404	-1.143	-0.0975	0.815e-3	-0.0654	0.991	4.179
MZI6	2.401	-1.146	-0.0676	0.664e-3	0.263	0.994	4.179
MZI7	2.403	-1.151	-0.0686	0.291e-3	0.299	0.993	4.191
MZI8	2.414	-1.137	0.0366	0.519e-3	-2.283	0.983	4.181

Table 5. Michelson interpolation data for effective index model extracted from measurements.

Label		n_1	n_2	n_3	α	b	R	n_g at $1.55\mu m$
Theory		2.449	-1.133	-0.775				4.204
Mich2	Loopback	2.420	-0.900	-2.744	4.792e-3	2.175	0.987	3.769
	Baseline	2.421	-0.614	-29.660	7.100e-3	1.991	0.867	2.486
Mich3	Loopback	2.410	-1.069	-0.0631	1.578e-3	2.001	0.990	4.075
	Baseline	2.410	-1.067	0.247	1.800e-3	-1.971	0.971	4.080
Mich4	Loopback	2.407	-1.098	-0.221	0.851e-3	1.862	0.990	4.112
	Baseline	2.404	-1.097	-0.126	0.900e-3	-2.320	0.985	4.111
Mich5	Loopback	2.408	-1.108	-0.0490	0.610e-3	1.762	0.986	4.132
	Baseline	2.405	-1.109	0.0071	0.600e-3	-2.547	0.981	4.134

Table 6. Free spectral range from theory, layout simulation and measurements.

Label	ΔL [μm]	FSR at $1.55\mu m$ [nm]			Relative error (%)
		Theory	Layout Simulation	Measurement	
RefTE	n/a	n/a	n/a	n/a	n/a
MZI1	0	0	0	0	0
MZI2	27.276	20.395	20.081	20.908	4.11
MZI3	64.374	8.967	8.728	8.908	2.06
MZI4	109.609	5.184	5.046	5.272	4.27
MZI5	160.890	3.439	3.563	3.596	0.92
MZI6	224.993	2.498	2.548	2.572	0.94
MZI7	423.921	1.343	1.347	1.364	0.74
MZI8	526.535	1.081	1.081	1.108	2.50
Mich1	0	0	0	0	0
Mich2	12.986	21.921	22.172	23.992	8.21
Mich3	32.226	8.562	8.623	9.228	7.02
Mich4	57.879	4.912	4.937	5.076	2.82
Mich5	83.533	3.408	3.015	3.512	5.47

7. Conclusions

This report presents the comprehensive process of simulating, designing, fabricating, measuring, and analyzing Mach-Zehnder (MZI) and Michelson interferometers in silicon-on-insulator (SOI) technology. The primary goal was to determine the measured free spectral range (FSR) of these interferometers and extract the guided index of the waveguides, critical parameters for evaluating device performance and fabrication accuracy.

The design was realized using the SiEPIC-EBeam-PDK Compact Model Library. Devices were fabricated using the NanoSOI MPW process by Applied Nanotools, employing direct-write electron beam lithography. Designs were optimized for TE-polarized modes using Lumerical MODE, Lumerical INTERCONNECT, and MATLAB, while KLayout was used for mask layout. Measurements were conducted with an automated test setup featuring grating couplers for efficient light coupling.

Special attention was given to manufacturing variability, with corner analysis and Monte Carlo simulations used to predict and quantify its effects. The corner analysis provided extreme cases of variability, while Monte Carlo simulations captured the probabilistic nature of fabrication deviations, enabling robust comparisons between designed and fabricated devices.

For MZI devices, loopback correction yielded excellent agreement between simulations and experimental data, with a minimal FSR error of 0.74%, well within the variability predicted by Monte Carlo simulations. The extracted effective index aligned with the corner analysis, revealing slight deviations caused by process tendencies to produce larger waveguides, resulting in higher group indices due to reduced confinement.

Michelson interferometers, particularly those with smaller path differences, showed greater deviations from expected values. These discrepancies were attributed to noisier measurement data, calibration challenges, and parasitic effects from the compact, meandered design. Although extending the maximum waveguide width to 615 nm in the corner analysis partially resolved the discrepancies, the compact Michelson design introduced additional dispersion and coupling losses, suggesting that alternative layouts might be more appropriate.

This report demonstrates the importance of a systematic workflow, from variability simulations to measurement analysis, for accurately characterizing and optimizing SOI photonic devices. The combined use of corner analysis and Monte Carlo simulations highlights the need for robust modeling and calibration techniques to ensure device performance and reliability amidst manufacturing variability.

Fabrication

The photonic devices were fabricated using the NanoSOI MPW fabrication process by Applied Nanotools Inc. (<http://www.appliednt.com/nanosoi>; Edmonton, Canada) which is based on direct-write 100 keV electron beam lithography technology. Silicon-on-insulator wafers of 200 mm diameter, 220 nm device thickness and 2 μ m buffer oxide thickness are used as the base material for the fabrication. The wafer was pre-diced into square substrates with dimensions of 25x25 mm, and lines were scribed into the substrate backsides to facilitate easy separation into smaller chips once fabrication was complete. After an initial wafer clean using piranha solution (3:1 H₂SO₄:H₂O₂) for 15 minutes and water/IPA rinse, hydrogen silsesquioxane (HSQ) resist was spin-coated onto the substrate and heated to evaporate the solvent. The photonic devices were patterned using a JEOL JBX-8100FS electron beam instrument at The University of British Columbia. The exposure dosage of the design was corrected for proximity effects that result from the backscatter of electrons from exposure of nearby features. Shape writing order was optimized for efficient patterning and minimal beam drift. After the e-beam exposure and subsequent development with a tetramethylammonium sulfate (TMAH) solution, the devices were inspected optically for residues and/or defects. The chips were then mounted on a 4" handle wafer and underwent an anisotropic ICP-RIE etch process using chlorine after qualification of the etch rate. The resist was removed from the surface of the devices using a

10:1 buffer oxide wet etch, and the devices were inspected using a scanning electron microscope (SEM) to verify patterning and etch quality. A 2.2 μm oxide cladding was deposited using a plasma-enhanced chemical vapour deposition (PECVD) process based on tetraethyl orthosilicate (TEOS) at 300°C. Reflectometry measurements were performed throughout the process to verify the device layer, buffer oxide and cladding thicknesses before delivery.

Measurements Description

To characterize the devices, a custom-built automated test setup [2, 6] with automated control software written in Python was used [3]. An Agilent 81600B tunable laser was used as the input source and Agilent 81635A optical power sensors as the output detectors. The wavelength was swept from 1500 to 1600 nm in 10 pm steps. A polarization maintaining (PM) fibre was used to maintain the polarization state of the light, to couple the TE polarization into the grating couplers [4]. A 90° rotation was used to inject light into the TM grating couplers [4]. A polarization maintaining fibre array was used to couple light in/out of the chip [5].

Acknowledgments

I/We acknowledge the edX UBCx Phot1x Silicon Photonics Design, Fabrication and Data Analysis course, which is supported by the Natural Sciences and Engineering Research Council of Canada (NSERC) Silicon Electronic-Photonic Integrated Circuits (SiEPIC) Program. The devices were fabricated by Richard Bojko at the University of Washington Washington Nanofabrication Facility, part of the National Science Foundation's National Nanotechnology Infrastructure Network (NNIN), and Cameron Horvath at Applied Nanotools, Inc. Omid Esmaeeli performed the measurements at The University of British Columbia. We acknowledge Lumerical Solutions, Inc., Mathworks, and KLayout for the design software.

Data Availability

All codes and data used to realize this report can be found at this link:

References

1. G.T. Reed, A.P. Knights. Silicon Photonics: An Introduction. Wiley, 2004.
2. R. Soref. The Past, Present, and Future of Silicon Photonics. *IEEE Journal of Selected Topics in Quantum Electronics* **12**, 6, 2006.
3. L. Chrostowski, M. Hochberg. Silicon Photonics Design. Cambridge University Press (CUP), 2015.
4. S. Shekhar, W. Bogaerts, L. Chrostowski, J. E. Bowers, M. Hochberg, R. Soref, B. J. Shastri. Roadmapping the next generation of silicon photonics. *Nat. Commun.* **15**, 751 (2024).
5. Y. Wang, X. Wang, J. Flueckiger, H. Yun, W. Shi, R. Bojko, N.A.F. Jaeger, L. Chrostowski. Focusing sub-wavelength grating couplers with low back reflections for rapid prototyping of silicon photonics circuit. *Opt. Express* **22**, 20652-20662 (2014).
6. D. Patel, V. Veerasubramanian, S. Ghosh, A. Samani, Q. Zhong, D. V. Plant. High-speed compact silicon photonic Michelson interferometric modulator. *Opt. Express* **22**, 26788-26802 (2014).
7. [Optical Simulation and Design Software | Ansys Optics](#)
8. [GitHub - SiEPIC/SiEPIC_EBeam_PDK: SiEPIC EBeam PDK & Library, for SiEPIC-Tools and KLayout](#)
9. [MODE - Finite Difference Eigenmode \(FDE\) solver introduction – Ansys Optics](#)
10. [KLayout Layout Viewer And Editor](#)
11. <http://siepic.ubc.ca/probestation>, using Python code developed by Michael Caverley.
12. <http://mapleleafphotonics.com>, Maple Leaf Photonics, Seattle WA, USA.
13. Z. Lu, J. Jhoja, J. Klein, X. Wang, A. Liu, J. Flueckiger, J. Pond, L. Chrostowski. Performance prediction for silicon photonics integrated circuits with layout-dependent correlated manufacturing variability. *Opt. Express* **25**, 9712-9733 (2017).